Progress In Electromagnetics Research, Vol. 123, 123–142, 2012

NONDESTRUCTIVE COMPLEX PERMITTIVITY AND PERMEABILITY EXTRACTION USING A TWO-LAYER DUAL-WAVEGUIDE PROBE MEASUREMENT GEOMETRY

M. D. Seal, M. W. Hyde*, and M. J. Havrilla

Air Force Institute of Technology, 2950 Hobson Way, Wright-Patterson AFB, OH 45433, USA

Abstract—A two-layer dual-waveguide probe measurement geometry is proposed to nondestructively measure the complex permittivity and permeability of planar materials. The new measurement structure consists of two rectangular waveguides attached to a PEC flange plate that is placed against the material under test, followed by a known material layer backed by a PEC. The purpose for this new measurement geometry is to improve the permittivity results obtained using the existing dual-waveguide probe geometries, namely, the PEC-backed and free-space-backed geometries, by permitting a larger electric field into the material under test and increasing the field coupling between the two rectangular waveguide apertures. The theoretical development of the technique is presented extending the existing single-layer PEC-backed method to the proposed two-layer dual-waveguide probe method. The new measurement structure is theoretically analyzed by replacing the waveguide apertures with equivalent magnetic currents as stipulated by Love's equivalence theorem. Making use of the magnetic-current-excited two-layer parallel-plate Green's function and enforcing the continuity of the transverse magnetic fields over the waveguide apertures results in a system of coupled magnetic field integral equations. These coupled magnetic field integral equations are then solved for the theoretical reflection and transmission coefficients using the Method of Moments. The desired complex permittivity and permeability of the material under test are found by minimizing the root-mean-square difference between the theoretical and measured reflection and transmission coefficients, i.e., numerical inversion. Last, experimental results utilizing the new two-layer technique are presented for two magnetic

Received 11 November 2011, Accepted 7 December 2011, Scheduled 14 December 2011

* Corresponding author: Milo Wilt Hyde (milo.hyde@afit.edu).

shielding materials and subsequently compared to the existing PEC-backed and free-space-backed dual-waveguide probe geometries.

1. INTRODUCTION

Waveguide probes, whether they be coaxial, rectangular, or circular, have numerous applications including nondestructive evaluation of solids and liquids [1–14], surface and subsurface crack detection [15–19], and even *in vivo* characterization of biological tissues [20, 21]. The majority of the published waveguide probe research deals with single probe geometries. The single probe geometry is well suited for the characterization of dielectric materials, e.g., biological specimens, plastics, ceramics, and most liquids; however, it suffers when one wants to fully characterize a magnetic material, such as a radio-frequency magnetic shielding material. This limitation prompted the development of techniques such as two-thickness method [14, 22–24], two-layer method [10, 11, 13, 24, 25], frequency-varying method [26], and the short/free-space method [10, 11, 13] to measure both permittivity ε_r and permeability μ_r using a single probe. However, these methods are not always applicable to a given measurement and may be numerically unstable [25].

Methods capable of obtaining both reflection S_{11} and transmission S_{21} coefficients simultaneously allow complex ε_r and μ_r values to be determined unambiguously at every data point due to the independence of S_{11} and S_{21}. Two measurement geometries have been published which exploit this technique, the flanged-waveguide measurement geometry using either rectangular [27] or coaxial waveguides [28] and the dual-waveguide probe (DWP) geometry [29].

The PEC-backed DWP geometry yielded accurate μ_r results, but had difficulty in determining ε_r [29]. The inaccurate ε_r results were due to the fact that since the PEC-backed material under test (MUT) is typically electrically thin and the predominately transverse electric field in the MUT region is forced to zero at the PEC walls of the MUT/parallel-plate region, only a small interrogating electric field exists in the MUT to measure permittivity. The opposite is true for the magnetic field in the MUT region, thus physically explaining the experimental results. To specifically address the PEC-backed DWP's ε_r-measurement sensitivity, a free-space-backed (FS-backed) DWP geometry was recently analyzed [30]. Intuitively, the FS-backed geometry should be the complement of the PEC-backed geometry, i.e., permit a large electric field and small magnetic field into the MUT region. It logically follows that this arrangement should yield more accurate ε_r while yielding less accurate μ_r values. However, the FS-

backed experimental results did not produce the expected improvement in ε_r due to insufficient coupling between the waveguide apertures, i.e., a substantial portion of the field was either reflected back from the aperture or radiated into the free-space region.

In this paper, a two-layer PEC-backed DWP geometry is proposed to improve the ε_r results over both existing PEC-backed and FS-backed geometries. In this geometry, the MUT is backed by a known material which is subsequently backed by a PEC (see Figure 1). This arrangement should allow a larger interrogating electric field into the MUT region (this of course depends on the electrical path length between the MUT and the PEC — $\lambda/4$ being ideal for this purpose) while providing the necessary coupling between the probes. In the next section, the measurement structure depicted in Figure 1 is theoretically analyzed. Like the PEC-backed and FS-backed geometries, this is accomplished by replacing the waveguide apertures with equivalent magnetic currents in accordance with Love's equivalence theorem [31, 32]. Enforcing the continuity of the transverse magnetic fields in the waveguide and parallel-plate regions at the waveguide apertures yields a set of coupled magnetic field integral equations (MFIEs). These MFIEs are then solved via the Method of Moments (MoM) [32, 33] for the theoretical S-parameters, S_{11}^{thy} and

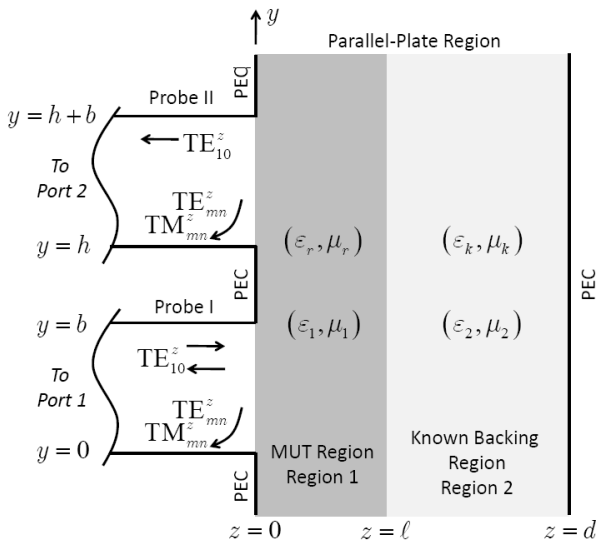

Figure 1. Two-layer PEC-backed dual-waveguide probe measurement geometry.

S_{21}^{thy}. The permittivity and permeability of the MUT are then found by solving the nonlinear system

$$\begin{aligned} \left| S_{11}^{\text{thy}}\left(f, d, \ell, \varepsilon_k, \mu_k; \varepsilon_r, \mu_r\right) - S_{11}^{\text{meas}}\left(f\right) \right| &\leqslant \delta \\ \left| S_{21}^{\text{thy}}\left(f, d, \ell, \varepsilon_k, \mu_k; \varepsilon_r, \mu_r\right) - S_{21}^{\text{meas}}\left(f\right) \right| &\leqslant \delta \end{aligned} \tag{1}$$

numerically. Here, δ is a user-defined tolerance and f is the frequency; the other symbols are defined pictorially in Figure 1. In Section 3, the new method is experimentally validated. Measurements are made of two magnetic shielding materials, ECCOSORB® FGM-125 and FGM-40 [34], each backed by acrylic ($\varepsilon_k \approx 2.6$, $\mu_k \approx 1$) and then a PEC. Last, this paper concludes with a summary of the work presented.

2. METHODOLOGY

2.1. System of Coupled MFIEs

The derivation of the theoretical coefficients S_{11}^{thy} and S_{21}^{thy} requires expressions for the transverse electric and magnetic fields in the waveguide/probe regions of Figure 1. In the probes, the fields may be expressed as a weighted summation of TE_{mn}^{z} and TM_{mn}^{z} rectangular waveguide modes [31]. In probe I, the transverse fields are comprised of an incident TE_{10}^{z} mode plus higher-order TE and TM reflected modes weighted by unknown and ultimately desired modal reflection coefficients Γ_{mn}^{TE} and Γ_{mn}^{TM}:

$$\begin{aligned} \mathbf{E}_t &= \mathbf{e}_{10}^{\text{TE}} e^{-\gamma_{10} z} + \sum_{m,n} \left(\Gamma_{mn}^{\text{TE}} \mathbf{e}_{mn}^{\text{TE}} + \Gamma_{mn}^{\text{TM}} \mathbf{e}_{mn}^{\text{TM}} \right) e^{\gamma_{mn} z} \\ \mathbf{H}_t &= \mathbf{h}_{10}^{\text{TE}} e^{-\gamma_{10} z} - \sum_{m,n} \left(\Gamma_{mn}^{\text{TE}} \mathbf{h}_{mn}^{\text{TE}} + \Gamma_{mn}^{\text{TM}} \mathbf{h}_{mn}^{\text{TM}} \right) e^{\gamma_{mn} z} \end{aligned}. \tag{2}$$

In probe II, the transverse fields are comprised of a sum of weighted transmitted modes, i.e.,

$$\begin{aligned} \mathbf{E}_t &= \sum_{m,n} \left(\mathrm{T}_{mn}^{\text{TE}} \mathbf{e}_{mn}^{\text{TE}} + \mathrm{T}_{mn}^{\text{TM}} \mathbf{e}_{mn}^{\text{TM}} \right) e^{\gamma_{mn} z} \\ \mathbf{H}_t &= -\sum_{m,n} \left(\mathrm{T}_{mn}^{\text{TE}} \mathbf{h}_{mn}^{\text{TE}} + \mathrm{T}_{mn}^{\text{TM}} \mathbf{h}_{mn}^{\text{TM}} \right) e^{\gamma_{mn} z} \end{aligned}. \tag{3}$$

Here, an $\exp\left(\mathrm{j}\omega t\right)$ time dependence is assumed and suppressed; $\mathbf{e}_{mn}^{\text{TE}}$, $\mathbf{e}_{mn}^{\text{TM}}$, $\mathbf{h}_{mn}^{\text{TE}}$, and $\mathbf{h}_{mn}^{\text{TM}}$ are the transverse electric and magnetic field distributions; Γ_{mn}^{TE}, Γ_{mn}^{TM}, $\mathrm{T}_{mn}^{\text{TE}}$, and $\mathrm{T}_{mn}^{\text{TM}}$ are the transverse electric and magnetic field reflection and transmission coefficients; and $\gamma_{mn} =$

$\left(k_x^2 + k_y^2 - k_0^2\right)^{1/2}$ is the z-directed propagation constant. Due to the symmetry of the TE_{10}^z incident field and the DWP geometry, only TE_{mn}^z and TM_{mn}^z modes of odd m index are excited [29]. Of these, the $\mathrm{TE}_{1n}^z/\mathrm{TM}_{1n}^z$ modes are most significant [29, 35].

The transverse magnetic field in the MUT region of Figure 1 is found by replacing the waveguide probe apertures with equivalent magnetic surface currents $\boldsymbol{\mathcal{M}}_1$ and $\boldsymbol{\mathcal{M}}_2$ via Love's equivalence principle [31, 32]. The transverse magnetic field is computed using these currents through the electric vector potential $\mathbf{F}$, i.e.,

$$\mathbf{H}_t^{\mathrm{pp}} = \frac{1}{\mathrm{j}\omega\mu_0\mu_r}\left(k_{\mathrm{MUT}}^2 + \nabla_t\nabla\cdot\right)\mathbf{F} \tag{4}$$

where

$$\begin{aligned}\mathbf{F} \;=\; & \int_0^b\int_0^a \bar{\mathbf{G}}\left(x,y,z|\,x',y',0\right)\cdot\boldsymbol{\mathcal{M}}_1\left(x',y'\right)dx'dy' \\ & + \int_h^{h+b}\int_0^a \bar{\mathbf{G}}\left(x,y,z|\,x',y',0\right)\cdot\boldsymbol{\mathcal{M}}_2\left(x',y'\right)dx'dy'.\end{aligned} \tag{5}$$

Note that $\bar{\mathbf{G}}$ is the dyadic Green's function for a magnetic-current-excited two-layer parallel-plate environment. In the DWP geometry analyzed in this paper, both the source and observation points are collocated in the MUT region of Figure 1. Thus, only that form (i.e., source in region 1, observer in region 1) of the Green's function is required. The derivation of the Green's function is provided in [36]. Only the relevant form needed for further theoretical analysis is provided here:

$$\begin{aligned}\tilde{\bar{\mathbf{G}}} &= \hat{\mathbf{x}}\tilde{G}_{xx}\hat{\mathbf{x}} + \hat{\mathbf{y}}\tilde{G}_{yy}\hat{\mathbf{y}} + \hat{\mathbf{z}}\left(\mathrm{j}\xi\tilde{G}_{zx}\hat{\mathbf{x}} + \mathrm{j}\eta\tilde{G}_{zy}\hat{\mathbf{y}} + \tilde{G}_{zz}\hat{\mathbf{z}}\right) \\ \tilde{G}_{\alpha\alpha}\left(\xi,\eta,z|z'\in[0,\ell]\right) &= \frac{\varepsilon_2 p_1 N_{\cosh}^{+} + \varepsilon_1 p_2 N_{\sinh}^{+}}{2p_1 D_t} \\ \tilde{G}_{zz}\left(\xi,\eta,z|z'\in[0,\ell]\right) &= \frac{\mu_1 p_2 N_{\cosh}^{-} + \mu_2 p_1 N_{\sinh}^{-}}{2p_1 D_n} \\ \tilde{G}_{z\alpha}\left(\xi,\eta,z|z'\in[0,\ell]\right) & \\ = \frac{p_1\left(\varepsilon_1\mu_1 - \varepsilon_2\mu_2\right)\sinh\left[2p_2\left(d-\ell\right)\right]\sinh\left(p_1 z\right)\cosh\left(p_1 z'\right)}{2p_1 D_t D_n} &\end{aligned} \tag{6}$$

Note that $\tilde{\bar{\mathbf{G}}}$ is the spectral-domain form of the Green's function; it is

related to the spatial form $\bar{\mathbf{G}}$ by

$$\bar{\mathbf{G}} = \frac{1}{(2\pi)^2} \int_{-\infty}^{\infty} \int_{-\infty}^{\infty} \bar{\bar{\mathbf{G}}} \left(\xi, \eta, z|z'\right) e^{\mathrm{j}\xi(x-x')} e^{\mathrm{j}\eta(y-y')} d\xi d\eta. \tag{7}$$

In (6), $\alpha = x, y$, $k_n = 2\pi f \left(\varepsilon_n \mu_n\right)^{1/2}$, and $p_n = \left(\xi^2 + \eta^2 - k_n^2\right)^{1/2}$ where $n = 1$ (MUT region) or $n = 2$ (known backing region), respectively. Also in (6),

$$\begin{aligned} N_{\cosh}^{\pm} &= \cosh[p_2(d-\ell)]\left\{\cosh\left[p_1\left(\ell - \left|z-z'\right|\right)\right] \pm \cosh\left[p_1\left(\ell - \left(z+z'\right)\right)\right]\right\} \\ N_{\sinh}^{\pm} &= \sinh[p_2(d-\ell)]\left\{\sinh\left[p_1\left(\ell - \left|z-z'\right|\right)\right] \pm \sinh\left[p_1\left(\ell - \left(z+z'\right)\right)\right]\right\} \\ D_t &= \varepsilon_2 p_1 \sinh(p_1\ell)\cosh[p_2(d-\ell)] + \varepsilon_1 p_2 \cosh(p_1\ell)\sinh[p_2(d-\ell)] \\ D_n &= \mu_1 p_2 \sinh(p_1\ell)\cosh[p_2(d-\ell)] + \mu_2 p_1 \cosh(p_1\ell)\sinh[p_2(d-\ell)] \end{aligned} \tag{8}$$

The system of coupled MFIEs is derived by enforcing continuity of transverse magnetic fields at the waveguide probe apertures:

$$\begin{aligned} \mathbf{h}_{10}^{\mathrm{TE}} - \sum_{m,n} \left(\Gamma_{mn}^{\mathrm{TE}} \mathbf{h}_{mn}^{\mathrm{TE}} + \Gamma_{mn}^{\mathrm{TM}} \mathbf{h}_{mn}^{\mathrm{TM}}\right) &= \mathbf{H}_t^{\mathrm{pp}}(x, y, 0) \quad x, y \in \text{probe I} \\ -\sum_{m,n} \left(\mathrm{T}_{mn}^{\mathrm{TE}} \mathbf{h}_{mn}^{\mathrm{TE}} + \mathrm{T}_{mn}^{\mathrm{TM}} \mathbf{h}_{mn}^{\mathrm{TM}}\right) &= \mathbf{H}_t^{\mathrm{pp}}(x, y, 0) \quad x, y \in \text{probe II} \end{aligned} \tag{9}$$

Note that the unknowns in the above system are $\boldsymbol{\mathcal{M}}_1$, $\boldsymbol{\mathcal{M}}_2$, $\Gamma_{mn}^{\mathrm{TE}}$, $\Gamma_{mn}^{\mathrm{TM}}$, $\mathrm{T}_{mn}^{\mathrm{TE}}$, and $\mathrm{T}_{mn}^{\mathrm{TM}}$.

2.2. MoM Solution

The MoM [32, 33] is employed to solve the system of coupled MFIEs in (9). The first step in the MoM is to expand the unknown currents in a set of basis functions. Note that the magnetic current density is related to the electric field by

$$\boldsymbol{\mathcal{M}} = -\hat{\mathbf{n}} \times \mathbf{E} \tag{10}$$

where $\hat{\mathbf{n}} = \hat{\mathbf{z}}$ in this application. It thus makes physical sense to choose the transverse electric field distributions given in (2) and (3) as basis functions for $\boldsymbol{\mathcal{M}}_1$ and $\boldsymbol{\mathcal{M}}_2$, respectively:

$$\begin{aligned} \boldsymbol{\mathcal{M}}_1 &= -\hat{\mathbf{z}} \times \left[\mathbf{e}_{10}^{\mathrm{TE}} + \sum_{m,n} \left(\Gamma_{mn}^{\mathrm{TE}} \mathbf{e}_{mn}^{\mathrm{TE}} + \Gamma_{mn}^{\mathrm{TM}} \mathbf{e}_{mn}^{\mathrm{TM}}\right)\right] \\ \boldsymbol{\mathcal{M}}_2 &= -\hat{\mathbf{z}} \times \left[\sum_{m,n} \left(\mathrm{T}_{mn}^{\mathrm{TE}} \mathbf{e}_{mn}^{\mathrm{TE}} + \mathrm{T}_{mn}^{\mathrm{TM}} \mathbf{e}_{mn}^{\mathrm{TM}}\right)\right] \end{aligned} \tag{11}$$

Substitution of (11) into (9) and subsequent simplification yields a $4 \times 4N$ system. In order to make the system full rank, the second step of the MoM is performed, namely, testing. Rectangular waveguide transverse magnetic field distributions are used as testing functions to take advantage of waveguide-mode orthogonality. The testing operation yields a $4N \times 4N$ system of equations, which may be represented in matrix form as $\mathbf{Ax} = \mathbf{b}$ where $\mathbf{A}$ is the MoM impedance matrix, $\mathbf{b}$ is a vector containing the contribution from the incident field, and $\mathbf{x}$ is a vector of the complex reflection and transmission coefficients.

2.3. Material Parameter Extraction

As with most material characterization methods, the notable exception being Nicolson, Ross, Weir (NRW) [37, 38], a closed-form expression for ε_r and μ_r in terms of S_{11} and S_{21} does not exist. It thus becomes necessary to perform the inversion numerically to extract ε_r and μ_r from the theoretical models. To mitigate the effects of noise, S_{12} and S_{22} are included in the system of nonlinear equations, namely,

$$\begin{aligned}
&\left|S_{11}^{\text{thy}}\left(f, d, \ell, \varepsilon_k, \mu_k; \varepsilon_r, \mu_r\right) - S_{11}^{\text{meas}}\left(f\right)\right| \leq \delta \\
&\left|S_{21}^{\text{thy}}\left(f, d, \ell, \varepsilon_k, \mu_k; \varepsilon_r, \mu_r\right) - S_{21}^{\text{meas}}\left(f\right)\right| \leq \delta \\
&\left|S_{12}^{\text{thy}}\left(f, d, \ell, \varepsilon_k, \mu_k; \varepsilon_r, \mu_r\right) - S_{12}^{\text{meas}}\left(f\right)\right| \leq \delta \\
&\left|S_{22}^{\text{thy}}\left(f, d, \ell, \varepsilon_k, \mu_k; \varepsilon_r, \mu_r\right) - S_{22}^{\text{meas}}\left(f\right)\right| \leq \delta
\end{aligned} . \tag{12}$$

Since the proposed system of equations is over determined a nonlinear least squares method, the Levenberg-Marquardt algorithm, is used to solve (12) to within a tolerance $\delta = 10^{-6}$ [39]. Note that $\Gamma_{10}^{\text{TE}} = S_{11}^{\text{thy}} = S_{22}^{\text{thy}}$ due to the symmetry of the measurement geometry and $\text{T}_{10}^{\text{TE}} = S_{21}^{\text{thy}} = S_{12}^{\text{thy}}$ due to reciprocity.

3. EXPERIMENTAL VERIFICATION

The DWP consists of two precision X-band rectangular waveguides connected with screws to a 30.48 cm $\times$ 30.48 cm $\times$ 9.779 mm aluminum flange plate (see Figure 2). To ensure sufficient coupling when measuring lossy materials, the rectangular waveguides are machined so that only a 3.810 mm space exists between their apertures. The measurement apparatus is calibrated using the Thru-Reflect-Line calibration method (TRL) [40] using specially machined line and short

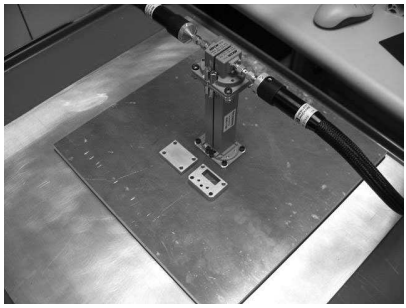

Figure 2. Photograph of the DWP measurement apparatus including specially machined line and short calibration standards.

standards. The TRL calibration places the forward and reverse phase-reference planes at the probe I and probe II rectangular waveguide apertures. To shift these calibration planes to the flange/material interface, an ideal phase delay, equal to twice the TE_{10}^{z} z-directed propagation constant γ_{10} times the aluminum flange plate thickness, is applied to the raw measured S-parameters, i.e.,

$$\begin{aligned} S_{11}^{\mathrm{meas}} &= S_{11}^{\mathrm{raw}} \exp\left(2\gamma_{10}\Delta\right) \\ S_{21}^{\mathrm{meas}} &= S_{21}^{\mathrm{raw}} \exp\left(2\gamma_{10}\Delta\right) \\ S_{12}^{\mathrm{meas}} &= S_{12}^{\mathrm{raw}} \exp\left(2\gamma_{10}\Delta\right) \\ S_{22}^{\mathrm{meas}} &= S_{22}^{\mathrm{raw}} \exp\left(2\gamma_{10}\Delta\right) \end{aligned} \tag{13}$$

where Δ is the flange plate thickness. To remove any possible reflections from the flange plate edges, the measured S-parameters are time gated as discussed in [41]. Also to minimize the effects of small air gaps which might exist between the flange plate and the MUT, approximately 18 kg of weight is applied to the top of the aluminum flange near where the rectangular waveguides attach to the plate during S-parameter measurements.

Material measurements at X-band (8.2 GHz to 12.4 GHz) of 3.175 mm thick ECCOSORB® FGM-125 and 1.016 mm thick ECCOSORB® FGM-40 [34] were made using an Agilent Technologies E8362B vector network analyzer (VNA) [42]. A 30.48 cm × 30.48 cm × 5.5 mm sample of acrylic ($\varepsilon_k \approx 2.6$, $\mu_k \approx 1$) was used as the known backing material in all measurements utilizing the two-layer DWP geometry. Acrylic is a rigid, low-loss, low-dispersion material making it very well suited to serve as a backing material. The ε_k and μ_k values for acrylic used in the extraction algorithm were determined using the standard NRW technique.

3.1. FGM-125 Results

The measured real and imaginary parts of both the permittivity ε_r [Figures 3(a) and 3(b)] and permeability μ_r [Figures 3(c) and 3(d)] of FGM-125 are shown in Figure 3. In the (a) and (c) subfigures, the PEC-backed (circle traces) and two-layer (square traces) DWP results are plotted; in the (b) and (d) subfigures, the two-layer (square traces) and FS-backed (triangle traces) DWP results are plotted. Each DWP geometry result has two traces associated with it — 1 and 5 $\mathrm{TE}^z_{1n}/\mathrm{TM}^z_{1n}$ higher-order modes traces denoted by different colors and line styles. For reference, the results using the industry standard NRW destructive characterization technique are also plotted. Complex permittivity and permeability for FGM-125 were also obtained using 10 higher-order modes. These traces are not included so as not to clutter Figure 3. Root-mean-square errors (RMSEs) of the PEC-backed, FS-backed, and two-layer DWP results (1, 5, and 10 higher-order modes) assuming the NRW results are the true values are reported in Table 1. Note that no real improvement in ε_r or μ_r accuracy results from including more than 5 higher-order modes implying solution convergence.

Certainly of note from the results presented in Figure 3 and Table 1 is that the ε_r results using the two-layer DWP geometry are significantly better than either the PEC-backed or FS-backed geometries, although the errors do become comparable as mode number increases for the PEC-backed results. The two-layer DWP ε_r improvement is physically expected considering that for the PEC-backed measurement, due to the distribution of the TE^z_{10} incident field and the relative thinness of the MUT, only a small interrogating electric field exists in the MUT region to probe the MUT's electrical properties. This is contrasted with the two-layer DWP which moves the MUT away from the PEC backing, thus changing the nature of the fields in the MUT region. Since the MUT is no longer backed by PEC, the interrogating electric field in the MUT region is much stronger than in the PEC-backed case, thus providing a more accurate and reliable ε_r measurement. In the case of μ_r, the results for the two-layer DWP are more error prone than the PEC-backed geometry. This result is also physically expected considering the behavior of the magnetic field in the two DWP geometries. For the PEC-backed measurement, the magnetic field in the MUT region can be expected to be large considering the proximity to the PEC boundaries. Thus, one would expect that the μ_r measurement would be accurate and reliable. Contrast this once again with the two-layer DWP geometry; the MUT is now located away from the PEC. While this action increases the strength of the electric field in the MUT region (as previously

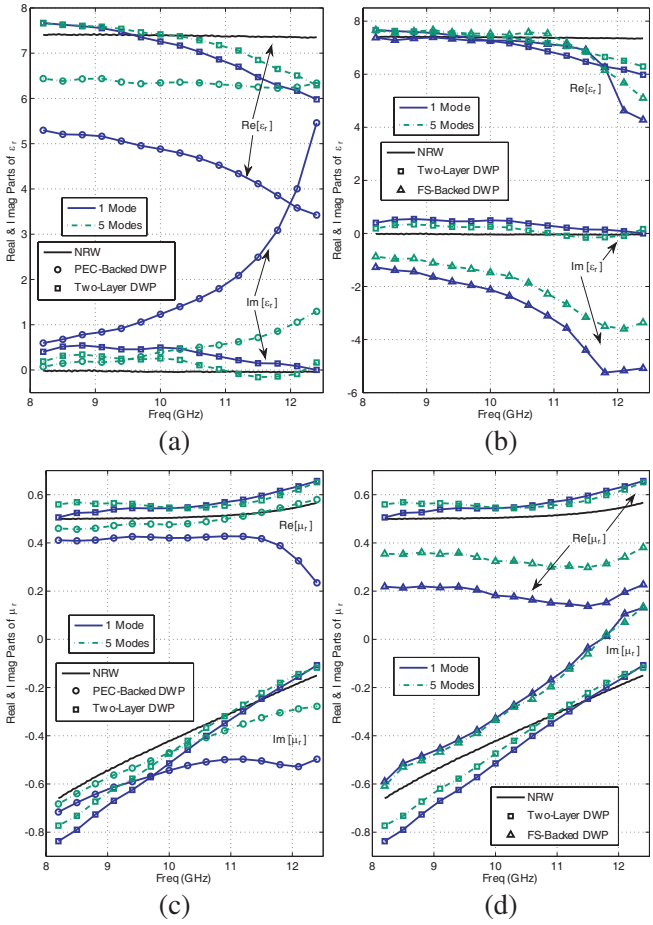

Figure 3. Complex permittivity ε_r results for FGM-125 using the PEC-backed (circle traces) and two-layer (square traces) DWP measurement geometries (1 and 5 modes traces are included). (b) Complex permittivity ε_r results for FGM-125 using the two-layer (square traces) and FS-backed (triangle traces) DWP measurement geometries (1 and 5 modes traces are included). (c) Complex permeability μ_r results for FGM-125 using the PEC-backed (circle traces) and two-layer (square traces) DWP measurement geometries (1 and 5 modes traces are included). (d) Complex permeability μ_r results for FGM-125 using the two-layer (square traces) and FS-backed (triangle traces) DWP measurement geometries (1 and 5 modes traces are included).

Table 1. PEC-Backed, FS-Backed, and Two-Layer DWP RMSEs for FGM-125.

	PEC-Backed DWP		
	1 Mode	5 Modes	10 Modes
Re $[\varepsilon_r]$	2.8407	1.0486	0.8491
Im $[\varepsilon_r]$	2.3300	0.6416	0.5974
Re $[\mu_r]$	0.1350	0.0253	0.0246
Im $[\mu_r]$	0.1957	0.0655	0.0531

	FS-Backed DWP		
	1 Mode	5 Modes	10 Modes
Re $[\varepsilon_r]$	1.1126	0.8152	0.7768
Im $[\varepsilon_r]$	3.1773	2.1899	2.0627
Re $[\mu_r]$	0.3298	0.1833	0.1683
Im $[\mu_r]$	0.1611	0.1493	0.1414

	Two-Layer DWP		
	1 Mode	5 Modes	10 Modes
Re $[\varepsilon_r]$	0.6508	0.4454	0.4225
Im $[\varepsilon_r]$	0.4095	0.2279	0.2043
Re $[\mu_r]$	0.0549	0.0574	0.0542
Im $[\mu_r]$	0.1018	0.0659	0.0575

discussed), this increase in electric field strength comes at the expense of the magnetic field. This explains the less accurate μ_r results for the two-layer DWP.

Applying the physical reasoning of the previous paragraph, one would expect that the two-layer DWP would perform about the same (perhaps a little worse) compared to the FS-backed geometry for ε_r and better for μ_r. However, as described in detail in [30], the FS-backed DWP suffers from poor probe coupling (highly dependent on the MUT), i.e., very little energy is transmitted from probe I, through the MUT, to probe II. This makes full electromagnetic characterization (determining ε_r and μ_r unambiguously) very difficult considering

that only the reflection measurements are viable. Note that it was this disappointing result which served as the impetus for the two-layer DWP geometry which confines the interrogating field between parallel, PEC plates thus significantly improving probe coupling, i.e., transmission.

3.2. FGM-40 Results

The measured real and imaginary parts of ε_r [Figure 4(a)] and μ_r [Figure 4(b)] for the thinner and more heavily loaded FGM-40 are shown in Figure 4. In the figures, both the two-layer (square traces) and FS-backed (triangle traces) DWP results are plotted. Note that the PEC-backed results are not presented because a solution to (12) is not found. FGM-40 is too electrically thin to numerically calculate the theoretical S-parameters using the PEC-backed DWP geometry. As is the case for the FGM-125 results, each DWP geometry has two traces associated with it, namely, 1 and 5 $\mathrm{TE}^z_{1n}/\mathrm{TM}^z_{1n}$ higher-order modes traces demarcated by different colors and line styles. The NRW results

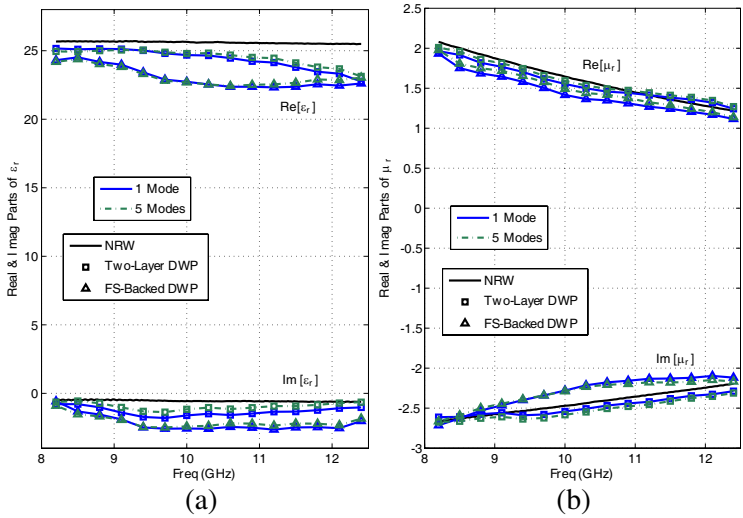

Figure 4. (a) Complex permittivity ε_r results for FGM-40 using the two-layer (square traces) and FS-backed (triangle traces) DWP measurement geometries (1 and 5 modes traces are included). (b) Complex permeability μ_r results for FGM-40 using the two-layer (square traces) and FS-backed (triangle traces) DWP measurement geometries (1 and 5 modes traces are included).

Table 2. FS-Backed and Two-Layer DWP RMSEs for FGM-40.

	FS-Backed DWP		
	1 Mode	5 Modes	10 Modes
$\mathrm{Re}\,[\varepsilon_r]$	2.6593	2.5588	2.4356
$\mathrm{Im}\,[\varepsilon_r]$	1.7189	1.5725	1.6265
$\mathrm{Re}\,[\mu_r]$	0.1799	0.1213	0.1117
$\mathrm{Im}\,[\mu_r]$	0.1546	0.1349	0.1381

	Two-Layer DWP		
	1 Mode	5 Modes	10 Modes
$\mathrm{Re}\,[\varepsilon_r]$	1.3815	1.1886	1.1060
$\mathrm{Im}\,[\varepsilon_r]$	0.8218	0.4611	0.4609
$\mathrm{Re}\,[\mu_r]$	0.0731	0.0524	0.0495
$\mathrm{Im}\,[\mu_r]$	0.0683	0.0973	0.0937

for FGM-40 are included on the figures as a reference. Table 2 reports the RMSEs of the FS-backed and two-layer DWP results assuming that the NRW ε_r and μ_r are the true values.

Inspection of the results presented in Figure 4 and Table 2 reveals that the two-layer DWP geometry improves upon the FS-backed geometry in every regard. As is the case for FGM-125 discussed in Section 3.1, the FS-backed DWP still experiences poor transmission; however, in this case, S_{21} is sufficiently above the VNA noise floor to yield results for ε_r and μ_r. However, since S_{21} is still very weak, the results are more error prone than the two-layer DWP geometry.

3.3. Combined Results

The last results presented in this paper are the combined DWP geometry results, i.e., the PEC-backed geometry combined with the two-layer and FS-backed DWP geometries. In these results,

$$\begin{aligned} \left|\mathbf{S}_{\mathrm{PEC}}^{\mathrm{thy}}\left(\varepsilon_r,\mu_r\right)-\mathbf{S}_{\mathrm{PEC}}^{\mathrm{meas}}\right| &\leqslant \delta \\ \left|\mathbf{S}_{\mathrm{TL}}^{\mathrm{thy}}\left(\varepsilon_r,\mu_r\right)-\mathbf{S}_{\mathrm{TL}}^{\mathrm{meas}}\right| &\leqslant \delta \end{aligned} \tag{14}$$

and

$$\begin{aligned}\left|\mathbf{S}_{\mathrm{PEC}}^{\mathrm{thy}}\left(\varepsilon_r,\mu_r\right)-\mathbf{S}_{\mathrm{PEC}}^{\mathrm{meas}}\right| &\leqslant \delta \\ \left|\mathbf{S}_{\mathrm{FS}}^{\mathrm{thy}}\left(\varepsilon_r,\mu_r\right)-\mathbf{S}_{\mathrm{FS}}^{\mathrm{meas}}\right| &\leqslant \delta\end{aligned} \tag{15}$$

are solved numerically (eight equations for two unknowns). Here, $\mathbf{S} = [S_{11} \quad S_{21} \quad S_{12} \quad S_{22}]^{\mathrm{T}}$, TL represents the two-layer DWP geometry, and FS represents the FS-backed DWP geometry. The impetus for combining the different DWP geometries in this manner arose from the analysis performed in [30]. Figure 5 shows the combined PEC-backed and two-layer DWP geometries (square traces) and the combined PEC-backed and FS-backed DWP geometries (triangle traces) ε_r [Figure 5(a)] and μ_r [Figure 5(b)] FGM-125 results for 1 and 5 $\mathrm{TE}_{1n}^{z}/\mathrm{TM}_{1n}^{z}$ higher-order modes (demarcated by different colors and line styles). Table 3 compares the RMSEs (FGM-125 NRW ε_r and μ_r

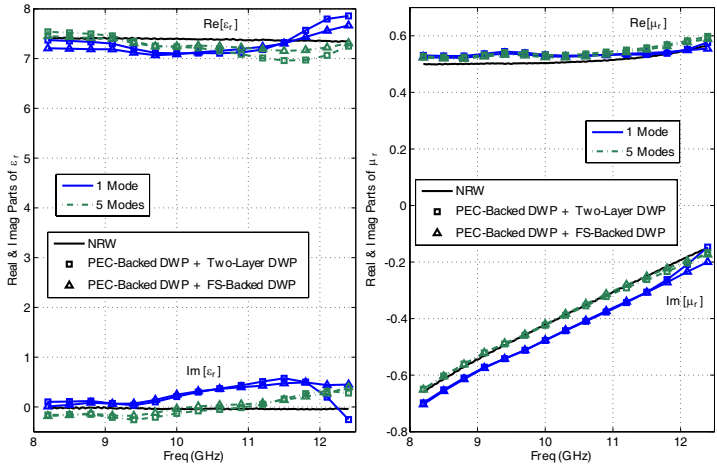

Figure 5. (a) Complex permittivity ε_r results for FGM-125 using S-parameter measurements collected from both the PEC-backed and two-layer (square traces) DWP measurement geometries and from both the PEC-backed and FS-backed (triangle traces) DWP measurement geometries (1 and 5 modes traces are included). (b) Complex permeability μ_r results for FGM-125 using S-parameter measurements collected from both the PEC-backed and two-layer (square traces) DWP measurement geometries and from both the PEC-backed and FS-backed (triangle traces) DWP measurement geometries (1 and 5 modes traces are included).

Table 3. Combined PEC-Backed and FS-Backed DWP and Combined PEC-Backed and Two-Layer DWP RMSEs for FGM-125.

	PEC-Backed & FS-Backed DWP		
	1 Mode	5 Modes	10 Modes
$\mathrm{Re}[\varepsilon_r]$	0.2302	0.1308	0.0774
$\mathrm{Im}[\varepsilon_r]$	0.3528	0.1893	0.1734
$\mathrm{Re}[\mu_r]$	0.0221	0.0236	0.0189
$\mathrm{Im}[\mu_r]$	0.0514	0.0092	0.0096

	PEC-Backed & Two-Layer DWP		
	1 Mode	5 Modes	10 Modes
$\mathrm{Re}[\varepsilon_r]$	0.2563	0.2320	0.1748
$\mathrm{Im}[\varepsilon_r]$	0.3388	0.1952	0.1763
$\mathrm{Re}[\mu_r]$	0.0256	0.0305	0.0259
$\mathrm{Im}[\mu_r]$	0.0477	0.0110	0.0095

results assumed to be the true values) for the combined PEC-backed and FS-backed DWP geometries with those of the combined PEC-backed and two-layer DWP geometries.

Comparison of the combined PEC-backed and two-layer DWP errors listed in Table 3 with those listed for the two-layer DWP in Table 1 implies that little is gained by using measurements from both PEC-backed and two-layer DWP geometries. This is in stark contrast to the combined PEC-backed and FS-backed ε_r and μ_r errors (listed in Table 3) which are much better than those reported using the FS-backed DWP alone (see Table 1 and [30]). Note that these results imply that while the PEC-backed and two-layer DWP measurements are different, no new information is gained (i.e., the measurements are not completely independent) and thus do not yield more accurate ε_r and μ_r results when combined in the manner outlined in (14). The opposite is true for the PEC-backed and FS-backed DWP measurements. These two measurements (analogous to the independent combination of PEC-backed and matched-termination-backed S_{11} waveguide measurements) provide new information thus yielding more accurate ε_r and μ_r values when combined in the manner specified by (15). Note that combined measurements of FGM-40 were

also made. However, like in [30], these results mirror the two-layer and FS-backed DWP ε_r and μ_r values reported in Figures 3 and 4 and Tables 1 and 2 because of the aforementioned difficulty in calculating theoretical S-parameters using the PEC-backed structure.

4. CONCLUSION

A nondestructive technique for determining the complex permittivity and permeability of a planar material using a two-layer dual-waveguide probe measurement geometry was presented. The impetus for this new dual-waveguide probe geometry was two fold. The first was to address the ε_r-measurement sensitivity experienced by the PEC-backed geometry [29] by displacing the MUT from the PEC by a known material thereby permitting a larger electric field interrogation of the MUT region. The second was to address the weak field coupling between waveguide probes experienced by the FS-backed geometry [30] by containing the measurement in a parallel-plate environment (see Figure 1). The experimental results clearly demonstrated the utility of this approach. Significant improvements in permittivity were observed using the two-layer geometry compared to both the PEC-backed and FS-backed geometries.

The views expressed in this paper are those of the authors and do not reflect the official policy or position of the U.S. Air Force, the Department of Defense, or the U.S. Government.

REFERENCES

1. Mostafavi, M. and W. C. Lan, "Polynomial characterization of inhomogeneous media and their reconstruction using an open-ended waveguide," *IEEE Trans. Antennas Propag.*, Vol. 41, No. 6, 822–824, 1993.
2. Sanadiki, B. and M. Mostafavi, "Inversion of inhomogeneous continuously varying dielectric profiles using open-ended waveguides," *IEEE Trans. Antennas Propag.*, Vol. 39, No. 2, 158–163, 1991.
3. Bois, K. J., A. Benally, and R. Zoughi, "Multimode solution for the reflection properties of an open-ended rectangular waveguide radiating into a dielectric half-space: The forward and inverse problems," *IEEE Trans. Instrum. Meas.*, Vol. 48, No. 6, 1131–1140, 1999.
4. Ganchev, S. I., S. Bakhtiari, and R. Zoughi, "A novel numerical technique for dielectric measurement of generally lossy

dielectrics," *IEEE Trans. Instrum. Meas.*, Vol. 41, No. 3, 361–365, 1992.

5. Folgerø, K. and T. Tjomsland, "Permittivity measurement of thin liquid layers using open-ended coaxial probes," *Meas. Sci. Technol.*, Vol. 7, No. 8, 1164, 1996, Available: http://stacks.iop.org/0957-0233/7/i=8/a=012.
6. Wu, M., X. Yao, and L. Zhang, "An improved coaxial probe technique for measuring microwave permittivity of thin dielectric materials," *Meas. Sci. Technol.*, Vol. 11, No. 11, 1617, 2000, Available: http://stacks.iop.org/0957-0233/11/i=11/a=311.
7. Wu, M., X. Yao, J. Zhai, and L. Zhang, "Determination of microwave complex permittivity of particulate materials," *Meas. Sci. Technol.*, Vol. 12, No. 11, 1932, 2001.
8. Shin, D. H. and H. J. Eom, "Estimation of dielectric slab permittivity using a flared coaxial line," *Radio Sci.*, Vol. 38, No. 2, 2003.
9. Olmi, R., M. Bini, R. Nesti, G. Pelosi, and C. Riminesi, "Improvement of the permittivity measurement by a 3D full-wave analysis of a finite flanged coaxial probe," *Journal of Electromagnetic Waves and Applications*, Vol. 18, 217–232, 2004.
10. Baker-Jarvis, J., M. D. Janezic, P. D. Domich, and R. G. Geyer, "Analysis of an open-ended coaxial probe with lift-off for nondestructive testing," *IEEE Trans. Instrum. Meas.*, Vol. 43, No. 5, 711–718, 1994.
11. Li, C. L. and K. M. Chen, "Determination of electromagnetic properties of materials using flanged open-ended coaxial probe — Full-wave analysis," *IEEE Trans. Instrum. Meas.*, Vol. 44, No. 1, 19–27, 1995.
12. Chang, C. W., K. M. Chen, and J. Qian, "Nondestructive measurements of complex tensor permittivity of anisotropic materials using a waveguide probe system," *IEEE Trans. Microwave Theory Tech.*, Vol. 44, No. 7, 1081–1090, 1996.
13. Tantot, O., M. Chatard-Moulin, and P. Guillon, "Measurement of complex permittivity and permeability and thickness of multilayered medium by an open-ended waveguide method," *IEEE Trans. Instrum. Meas.*, Vol. 46, No. 2, 519–522, 1997.
14. Chang, C. W., K. M. Chen, and J. Qian, "Nondestructive determination of electromagnetic parameters of dielectric materials at X-band frequencies using a waveguide probe system," *IEEE Trans. Instrum. Meas.*, Vol. 46, No. 5, 1084–1092, 1997.

15. Yeh, C. Y. and R. Zoughi, "A novel microwave method for detection of long surface cracks in metals," *IEEE Trans. Instrum. Meas.*, Vol. 43, No. 5, 719–725, 1994.
16. Huber, C., H. Abiri, S. I. Ganchev, and R. Zoughi, "Modeling of surface hairline-crack detection in metals under coatings using an open-ended rectangular waveguide," *IEEE Trans. Microwave Theory Tech.*, Vol. 45, No. 11, 2049–2057, 1997.
17. Nadakuduti, J., G. Chen, and R. Zoughi, "Semiempirical electromagnetic modeling of crack detection and sizing in cement-based materials using near-field microwave methods," *IEEE Trans. Instrum. Meas.*, Vol. 55, No. 2, 588–597, 2006.
18. Mazlumi, F., S. H. H. Sadeghi, and R. Moini, "Interaction of an open-ended rectangular waveguide probe with an arbitrary-shape surface crack in a lossy conductor," *IEEE Trans. Microwave Theory Tech.*, Vol. 54, No. 10, 3706–3711, 2006.
19. McClanahan, A., S. Kharkovsky, A. R. Maxon, R. Zoughi, and D. D. Palmer, "Depth evaluation of shallow surface cracks in metals using rectangular waveguides at millimeter-wave frequencies," *IEEE Trans. Instrum. Meas.*, Vol. 59, No. 6, 1693–1704, 2010.
20. Bao, J. Z., S. T. Lu, and W. D. Hurt, "Complex dielectric measurements and analysis of brain tissues in the radio and microwave frequencies," *IEEE Trans. Microwave Theory Tech.*, Vol. 45, No. 10, 1730–1741, 1997.
21. Popovic, D., L. McCartney, C. Beasley, M. Lazebnik, M. Okoniewski, S. C. Hagness, and J. H. Booske, "Precision open-ended coaxial probes for *in vivo* and *ex vivo* dielectric spectroscopy of biological tissues at microwave frequencies," *IEEE Trans. Microwave Theory Tech.*, Vol. 53, No. 5, 1713–1722, 2005.
22. Chen, C. P., Z. Ma, T. Anada, and J.-P. Hsu, "Further study on two-thickness-method for simultaneous measurement of complex EM parameters based on open-ended coaxial probe," *Proceedings of the European Microwave Conference*, October 2005.
23. Stewart, J. W. and M. J. Havrilla, "Electromagnetic characterization of a magnetic material using an open-ended waveguide probe and a rigorous full-wave multimode model," *Journal of Electromagnetic Waves and Applications*, Vol. 20, No. 14, 2037–2052, 2006.
24. Maode, N., S. Yong, Y. Jinkui, F. Chenpeng, and X. Deming, "An improved open-ended waveguide measurement technique on parameters ε_r and μ_r of high-loss materials," *IEEE Trans. Instrum. Meas.*, Vol. 47, No. 2, 476–481, 1998.

25. Dester, G. D., E. J. Rothwell, M. J. Havrilla, and M. W. Hyde IV, "Error analysis of a two-layer method for the electromagnetic characterization of conductor-backed absorbing material using an open-ended waveguide probe," *Progress In Electromagnetics Research B*, Vol. 26, 1–21, 2010.
26. Wang, S., M. Niu, and D. Xu, "A frequency-varying method for simultaneous measurement of complex permittivity and permeability with an open-ended coaxial probe," *IEEE Trans. Microwave Theory Tech.*, Vol. 46, No. 12, 2145–2147, 1998.
27. Hyde, M. W. and M. J. Havrilla, "A nondestructive technique for determining complex permittivity and permeability of magnetic sheet materials using two flanged rectangular waveguides," *Progress In Electromagnetics Research*, Vol. 79, 367–386, 2008.
28. Baker-Jarvis, J. and M. D. Janezic, "Analysis of a two-port flanged coaxial holder for shielding effectiveness and dielectric measurements of thin films and thin materials," *IEEE Trans. Electromagn. Compat.*, Vol. 38, No. 1, 67–70, 1996.
29. Hyde, M. W., J. W. Stewart, M. J. Havrilla, W. P. Baker, E. J. Rothwell, and D. P. Nyquist, "Nondestructive electromagnetic material characterization using a dual waveguide probe: A full wave solution," *Radio Sci.*, Vol. 44, No. RS3013, 2009.
30. Hyde, M. W., M. J. Havrilla, A. E. Bogle, and E. J. Rothwell, "Nondestructive material characterization of a free-space-backed magnetic material using a dual-waveguide probe," *IEEE Trans. Antennas Propag.*, In Press, 2011, Available: http://ieeexplore.ieee.org/stamp/stamp.jsp?tp=&arnumber=6058602&isnumber=4907023.
31. Collin, R. E., *Field Theory of Guided Waves*, 2nd edition, IEEE Press, New York, 1991.
32. Peterson, A. F., S. L. Ray, and R. Mittra, *Computational Methods for Electromagnetics*, IEEE Press, New York, 1998.
33. Harrington, R., *Field Computation by Moment Methods*, IEEE Press, New York, 1993.
34. Emerson & Cuming Microwave Products, Inc., "ECCOSORB® FGM Permittivity & Permeability Data," 2007, Available: http://www.eccosorb.com/Collateral/Documents/English-US/Electrical%20Parameters/FGM%20Electrical%20Parameters.pdf.
35. Dester, G. D., E. J. Rothwell, and M. J. Havrilla, "An extrapolation method for improving waveguide probe material characterization accuracy," *IEEE Microwave Wireless Compon. Lett.*, Vol. 20, No. 5, 298–300, 2010.

36. Hyde, M. W. and M. J. Havrilla, "Electromagnetic characterization of two-layer dielectrics using two flanged rectangular waveguides," *Proceedings of the IEEE Instrumentation and Measurement Technology Conference*, 1648–1652, 2008.
37. Nicolson, A. M. and G. F. Ross, "Measurement of the intrinsic properties of materials by time-domain techniques," *IEEE Trans. Instrum. Meas.*, Vol. 19, No. 4, 377–382, 1970.
38. Weir, W. B., "Automatic measurement of complex dielectric constant and permeability at microwave frequencies," *Proc. IEEE*, Vol. 62, No. 1, 33–36, 1974.
39. Madsen, K., H. B. Nielsen, and O. Tingleff, *Methods for Nonlinear Least Squares Problems*, Technical University of Denmark, 2004.
40. Engen, G. F. and C. A. Hoer, "Thru-reflect-line: An improved technique for calibrating the dual six-port automatic network analyzer," *IEEE Trans. Microwave Theory Tech.*, Vol. 27, No. 12, 987–993, 1979.
41. Hyde, M. W., M. J. Havrilla, and A. E. Bogle, "A novel and simple technique for measuring low-loss materials using the flanged-waveguide measurement geometry," *Meas. Sci. Technol.*, Vol. 22, No. 8, 085704, 2011.
42. Agilent Technologies, Inc., "Technical specifications Agilent Technologies PNA series network analyzers E8362B/C, E8363B/C, and E8364B/C," 2008.